UNIVERSIDAD DE ZARAGOZA
FACULTAD DE CIENCIAS

TRABAJO DE FIN DE GRADO
GRADO EN MATEMÁTICAS

Fourier Transform based algorithms for data inversion taken with Coherent X-ray microscopy

---

Autora:
Laura Navarro Cozcolluela

Directora:
Irene Calvo Almazán

Noviembre de 2024

Contents

Resumen en castellano

Uno de los desarrollos científicos más revolucionarios que han tenido lugar en el ámbito de rayos-X es la imagen por difracción coherente (*Coherent Diffraction Imaging, CDI*). Al contrario de la microscopía tradicional, donde se hace uso de lentes para recoger la luz dispersada por una muestra, y así recuperar la imagen, CDI ilumina directamente la muestra con un haz coherente y recoge la luz difractada por el objeto en un detector. De este modo, elimina todas las limitaciones que introducen las lentes, permitiendo su uso en numerosas aplicaciones, como la visualización detallada en tres dimensiones (3D) de los componentes básicos en materiales o células. En este trabajo nos centraremos en el modo de medir conocido como Bragg CDI (BCDI). Consiste en realizar la medida CDI en geometría de Bragg, es decir, iluminando la muestra tal que la dirección del haz incidente y el difractado coincidan con un pico de Bragg, producido por una familia de planos específicos dentro del cristal. Además, para obtener informactión en 3D se realiza una medida llamada *rocking curve scan*, que consiste en rotar ligeramente (en una ventana angular de $\sim 1°$) el cristal con respecto a la dirección del haz incidente y así, medir la distribución 3D de intensidad difractada en torno al pico de Bragg.

Para recuperar la imagen del objeto a partir de las medidas de en 3D de la intensidad difractada, se hace un procesado numérico de los datos. Dicho procesado se basa en que la onda difractada por la muestra (que es una magnitud compleja y por tanto tiene módulo y fase) es proporcional a la Transformada de Fourier (FT, del inglés *Fourier Transform*) de la densidad electrónica del objeto. Esto ocurre únicamente al tener un haz coherente, de aquí la importancia de este factor. Sin embargo, como sólo la intensidad, es decir, el módulo al cuadrado de la FT, puede ser medida por un detector, la información de fase se pierde, conduciendo al conocido como problema de la fase. Sin embargo, la distribución de fase de la onda difractada que falta y, por tanto, el frente de onda completo, puede obtenerse mediante un algoritmo siempre y cuando la distribución de intensidad obtenida esté lo suficientemente muestreada (este concepto se desarrollará en detalle).

Los algoritmos de recuperación de fase funcionan relacionando iterativamente el espacio real y el espacio recíproco a través de la Transformada de Fourier. En cada ciclo, el algoritmo propone un *ansazt* (una hipótesis para el modulo y fase del campo difractado y para el correspondiente objeto) y aplica en el espacio real distintas restricciones, como el soporte, la positividad (que indica que la densidad de electrones no puede ser negativa) o las regiones parcialmente superpuestas, mientras que la intensidad medida se utiliza como restricción en el espacio recíproco. Normalmente, después de varios cientos a miles de iteraciones, se puede recuperar la información de fase exacta, como se explicará en detalle en la Sección 3. La base teórica necesaria para establecer la viabilidad de la reconstrucción fue propuesta por Sayre en 1952. En esencia, fue el primero en asociar una función periódica junto con su FT y los espectros en el dominio de la frecuencia a un cristal y la intensidad difractada en el campo recíproco.

No obstante, estos algoritmos tienen algunas limitaciones: todos asumen que la muestra está estática. Además, el objeto no debe rotar durante las medidas, para no introducir una fuente de incertidumbre adicional en la *rocking curve* que afecte a la calidad de la reconstrucción del objeto. Sin embargo, en un experimento, la estática del objeto no siempre puede garantizarse, lo que provoca problemas de reconstrucción y requiere entonces el desarrollo de nuevas estrategias para superarlos.

Este trabajo está dividido en cuatro secciones: en la Sección 2 se describe el fundamento teórico necesario para desarrollar los algoritmos de reconstrucción, en la Sección 3 demostraremos la capacidad de los algoritmos de reconstrucción estándar para recuperar la forma y la estructura interna (es decir, el módulo y la fase) de un cristal cúbico ideal y en la Sección 4 ilustraremos las limitaciones del algoritmo anterior, basado en la Transformada de Fourier 3D, en un experimento más realista en el que el cristal simulado está rotado respecto al haz entrante. Así, surge de manera natural la necesidad de un nuevo algoritmo de reconstrucción basado en el Teorema de "corte"de Fourier (*Fourier Slice Theorem*), que explicaremos y aplicaremos. Por último, en la Sección 5 presentaremos las conclusiones obtenidas y propondremos nuevas líneas de trabajo futuro.

En primer lugar, la Sección 2 desarrolla el fundamento teórico, tanto de la Transformada de Fourier como sus aplicaciones al campo de imagen difractada y los algoritmos que la utilizan. Comenzaremos definiendo una sucesión periódica, y sobre ella, la Transformada Discreta de Fourier y su inversa. No obstante, si el número de datos que tenemos es muy grande, el número de operaciones a realizar crece, y con él, también el tiempo de cómputo, por lo que muchos resultados no podían calcularse. Para solucionar este problema surge el algoritmo de la Transformada Rápida de Fourier (FFT, del inglés *Fast Fourier Transform*). En esta línea, se realiza un estudio exhaustivo del número de operaciones necesario, antes y después de la introducción de la FFT, mostrando de forma clara las ventajas y necesidad de este nuevo algoritmo.

A continuación, esta definición matemática de la FT se conecta con el formalismo utilizado en la obtención de imágenes por difracción coherente. En esta línea, se explica cómo las características de la FT conducen a las propiedades de los campos real y difractado, y se aborda el problema de la fase, detallando las ligaduras que requiere. Posteriormente, se explican varios algoritmos de recuperación de fase: *Error-Reduction* (ER), *Hybrid-Input-Output* (HIO) y *Shrink-Wrap* (SW). Sin embargo, estos algoritmos tienen un denominador común que es la suposición de que el objeto está estático. Por lo tanto, cuando esto no se cumple, requiere un nuevo planteamiento del problema, que se resuelve introduciendo el *Fourier Slice Theorem*. Esta nueva estrategia algorítmica abre la puerta de aplicar Bragg CDI al estudio de sistemas que evolucionan en el tiempo.

En la Sección 3 se reconstruye un cristal cúbico ideal utilizando algoritmos estándar de recuperación de la fase. En primer lugar, simularemos un cristal cúbico ideal, esto es, sin rotaciones o efectos indeseados en la medida. A él le aplicaremos la FT para obtener su patrón de difracción (DP, del inglés *Diffraction Pattern*) asociado, es decir, la intensidad que seríamos capaces de medir en el laboratorio. Es a este DP a quien le aplicaremos el algoritmo propuesto.

Este algoritmo consta de un total de 560 iteraciones, organizadas en cinco ciclos de ER + HIO, finalizando con 200 iteraciones de ER, para asegurar que la métrica de error alcanza su mínimo. Además, a mitad de cada serie de ER se actualiza el soporte vía SW. Para mostrar la actuación del algoritmo, se presenta la evolución de la métrica de error a lo largo de cada una de las iteraciones, evidenciando el efecto de cada uno de los algoritmos individuales.

Haciendo uso de este algoritmo, trataremos de reconstruir el objeto simulado al principio del capítulo. Para enseñar la evolución del objeto y cómo varía a lo largo de cada una de las iteraciones, se representan y explican, tanto el módulo como la fase del objeto, en las cuatro fases del algoritmo de la última iteración, evidenciando así el efecto directo de la FT en la reconstrucción.

En la Sección 4, por otro lado, simularemos un experimento más realista. Para ello, rotaremos el cubo cristalino con respecto a la dirección angular incidente un ángulo θ. El mero hecho de rotar el cristal hace que los planos del detector estén inclinados con respecto a la dirección de Q_{HKL}, introduciendo un artefacto en la imagen. Además, para hacer el experimento aún más realista, incluiremos una incertidumbre angular -a la que llamaremos *jitter*-, para simular rotaciones incontroladas del cristal durante la medida (como ocurriría en el caso de un aumento en la temperatura del cristal), y ruido de Poisson, para reproducir de forma más precisa el proceso de detección de los fotones por un detector, que es en esencia estocástico.

Para corregir estos efectos en la calidad de la reconstrucción, y en particular el de las rotaciones incontroladas del cristal, se propone una modificación del algoritmo, sustituyendo la FT en 3D por una serie de FTs en 2D, según el *Fourier Slice Theorem.* Sin embargo, no se han procesado los datos a través de un algoritmo, por lo que se ha estudiado esta herramienta para invertir los datos y observar la imagen que un algoritmo que la utilice podría, potencialmente, reconstruir.

Se muestra entonces la evolución, tanto de la correlación entre el objeto original y el objeto recuperado por FT en 3D y por FT en 2D mediante el *Fourier Slice Theorem*, para diferentes grados de *jittering*, como de las distribuciones obtenidas del objeto invertido en el espacio real. Esto demuestra la necesidad de introducir este nuevo enfoque de la FT en 2D, así como de extraer las conclusiones adecuadas, prestando atención a los parámetros obtenidos numéricamente y a las gráficas de los objetos.

Por último, en la Sección 5 se concluye el trabajo realizado, tratando de explicar los artefactos que aparecen en las imágenes obtenidas de los objetos en relación a las limitaciones del algoritmo utilizado. Además, también se proponen líneas de trabajo futuro, continuando con el trabajo que se ha llevado a cabo.

1 Introduction

One of the most revolutionary developments that the X-ray science community has witnessed over the past two decades is coherent diffractive imaging (CDI), a new approach to X-ray crystallography that enables structure determination of noncrystalline specimens and nanocrystals with a resolution limited only by the spatial frequency of the diffracted waves. It emerged from the realization that finely sampled ("oversampled") diffraction patterns (DP) can be inverted to obtain real space images [1].

Unlike traditional microscopy, where a lens is used to collect the light scattered by a sample and thereby recover an image, CDI avoids the physical and geometrical limitations that lenses introduce by illuminating an object with a coherent laser-like beam and collecting the scattered light on a detector. Just because no optics is inserted between the sample and the detector, CDI represents the most photon-efficient X-ray imaging modality. CDI is ideally suited for non-destructive, quantitative 3D characterization of materials at the nanoscale: X-rays have a larger penetration depth than electrons, so that destructive sample preparation can often be avoided. Also, CDI can extract the mass density and thus distinguish different phases in materials in three dimensions. Furthermore, it enables nanoscale chemical, elemental, and magnetic mapping of complex matter, allowing the internal structure of crystals and their irregular morphology to be seen. In biological applications, CDI offers three distinctive features: it can image entire cells without sectioning due to high X-ray penetration, utilizes the intrinsic density phase shift (contrast) for detailed 3D imaging of cells and organelles, and achieves high resolution (in the range of nanometers) as it is limited only by the spatial frequency of the diffracted waves, rather than by lens limitations [2, 3].

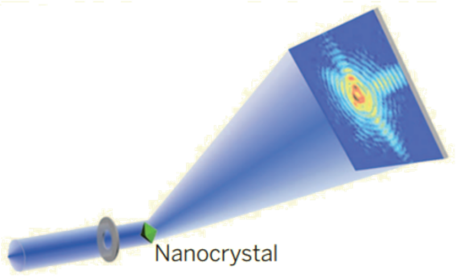

Figure 1: *Schematic layout of Bragg CDI: A coherent X-ray beam illuminating a nanocrystal and its diffraction pattern surrounding a Bragg peak. Figure extracted from [2].*

In this work, we will focus on an implementation of CDI which serves to visualize individual 3D crystalline objects and which is called Bragg CDI (BCDI), as shown in Figure 1 . It consists in performing a CDI experiment in Bragg geometry (see Panel a) of Figure 2): this is, to illuminate with a coherent X-ray beam (i.e. a plane wave in the first approximation) an individual crystal such that the incident and exit directions of the beam, $\mathbf{k_i}$ and $\mathbf{k_f}$ respectively, match the "Bragg condition". This happens when the momentum transfer, defined as $\mathbf{Q} = \mathbf{k_f} - \mathbf{k_i}$, points at a specific Bragg peak associated to a specific family of planes within the crystal, that we label with the Miller indexes (HKL). In that case, the intensity registered in the detector corresponds to a cut through the intensity distribution around that Bragg peak (see Panel b) of Figure 2). Then, to gather 3D structural information, we need to perform a "rocking curve scan". This consists in rocking the sample (i.e. slightly change the orientation of the crystal) with respect to the incoming beam direction such that we register with the detector a series of parallel cuts of intensity around the 3D Bragg peak (see Panel c) of Figure 2). The rocking curve scan yields a 3D data set which can be finally processed by a numerical algorithm to obtain a reconstruction of the crystalline system.

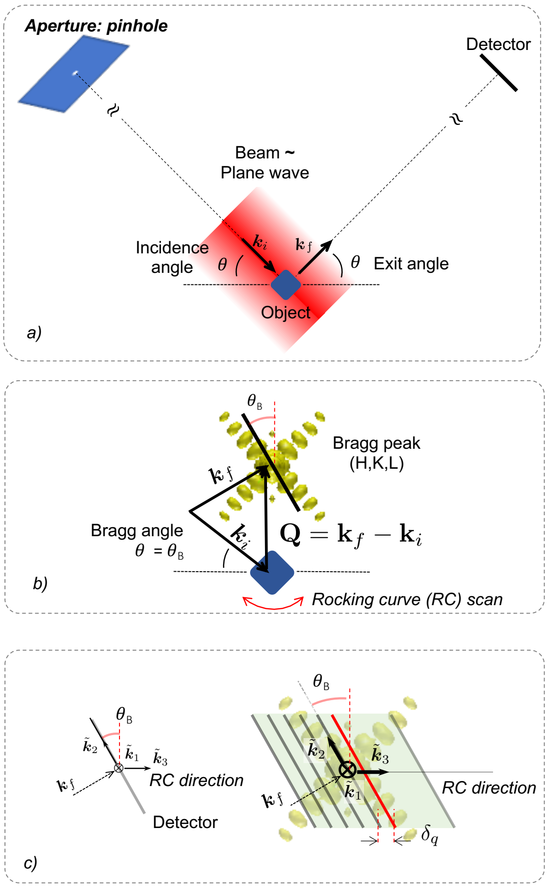

Figure 2: *Schematics to illustrate the basic concepts of Bragg CDI: a) Bragg geometry measurements, b) "Bragg condition" and c) rocking curve. Figure extracted from [4].*

Then, the image is recovered through the numerical processing of the data set, which exploits the fact that the complex diffracted wave is proportional to the Fourier Transform (FT) of the electron density of the object. Note that a necessary condition for this to occur is to have a coherent beam, hence the importance of this factor. However, since only the intensity, that is, the magnitude squared of the FT, can be measured by a detector, the phase information is lost. This loss leads to the phase problem, where the missing phase information complicates the reconstruction of an image from a diffraction pattern. If the complex-valued distribution of the scattered wavefront was available, a simple inverse FT could yield the exact sample distribution. In reality, though, only the intensity distribution can be measured, which provides only the amplitude distribution of the scattered wave. Despite this, the missing phase distribution of the scattered wave and thus the complete wavefront can be retrieved through an algorithm, as long as the acquired intensity distribution is sufficiently fine-sampled ("oversampled", we will develop this concept further below) [5].

Phase retrieval algorithms operate by iteratively switching between real space and reciprocal space. In each cycle, different constraints are applied to a *guessed* object, such as support, positivity (indicating that electron density cannot be negative) or partially overlapping regions, are applied in real space, while the measured Fourier magnitude is used as a constraint in reciprocal space. Typically, after several hundred to thousands of iterations, the guessed object is refined until its corresponding diffraction pattern is congruent with the experimental one and then, we consider that the accurate phase information has been recovered, as will be explained in detail in Section 3.

However, the success of the data-processing stage depends not only on the convergence properties of algorithms but also on a foundational body of theory that establishes the feasibility of reconstructions. In 1952, David Sayre, influenced by Shannon's sampling theorem [6], wrote a brief paper [7] recognized as the first to propose the concept of diffractive imaging. In essence, he was the first to associate a periodical function together with its Fourier transform and the spectra in the frequency domain to a crystal and the diffracted intensity in the reciprocal field.

Nevertheless, these algorithms have some limitations. In the time frame over which an individual rocking curve is measured, the sample is assumed to be static: i.e. nor its internal structure, nor its morphology change. In addition, the object should not rotate during the rocking curve, such that we can assume that the detector planes measure, in fact, a series of 2D planes on a regular grid (i.e. they are equispaced). However, in a experiment, the static object constraint cannot always be ensured, leading to reconstruction problems. Throughout this work we will show how phase retrieval algorithms work in the ideal case, but also the problems that can be faced in the aforementioned real situations and some strategies will be proposed to overcome them.

This work is divided in four sections:

- First of all, the theoretical framework is described. We will begin explaining the mathematical concepts of the Discrete Fourier Transform and the Fast Fourier Transform, emphasizing the need for such an algorithm. Once these concepts have been introduced, they will be connected to the CDI theory and the phase problem will be explained, as well as the constraints that its solution requires. Afterwards, the standard phase retrieval algorithms will be described, as well as how they apply these constraints. Finally we will discuss the limitations of these algorithms, specially in the context of real experiments, and the need for new strategies based on the Fourier slice theorem.

- In second place, we will demonstrate the ability of standard reconstruction algorithms, to retrieve the shape and the internal structure (i.e. the modulus and phase) of an ideal cubic crystal. For this, we will simulate the diffracted intensity produced by that sample and measured over the course of a rocking curve scan and we will invert it with an algorithm implemented to recover the original crystal. This proposed algorithm consists of a combination of three standard algorithms used for phase retrieval: Error-Reduction, Hybrid-Input-Output and Shrink-Wrap. The step-by-step evolution of the object throughout the algorithm will be presented, as well as the progression of the error metric, showing the effects of each of the series.

- Lastly, we will illustrate the limitations of the previous algorithm based on the 3D Fourier transform in a more realistic experiment where the simulated crystal is rotated with respect to the incoming beam. In this case, the need of a different algorithm, based on the Fourier Slice Theorem is explained and applied, and its effect on data inversion was compared to the 3D IFFT previously employed.

2 Theoretical framework

2.1 Discrete Fourier Transform

The discrete Fourier Transform transforms a set of N complex numbers $\{x_n\} := x_0, x_1, \dots, x_{N-1}$ into another set of complex numbers, $\{X_k\} := X_0, X_1, \dots, X_{N-1}$, making use of exponentials as will be seen [8]. Due to the periodicity of these exponentials, the most appropriate context to develop this theory is that of periodic sequences. Thus, we define the following:

Definition 2.1.1. *A sequence of complex numbers $a = \{a_n\}_{n\in\mathbb{Z}}$ is said to be N-periodic if*

$$a_{n+N} = a_n, \quad \forall n \in \mathbb{Z}.$$

Definition 2.1.2. *Given an N-periodic sequence $\mathbf{b} = \{b_n\}_{n\in\mathbb{Z}}$, we call the* ***discrete Fourier Transform (N)*** *of* $\mathbf{b}$ *the sequence with coefficients*

$$c_k = \sum_{n=0}^{N-1} b_n e^{-2\pi i n \frac{k}{N}} = \sum_{n=1}^{N} b_{j_n} e^{-2\pi i j_n \frac{k}{N}}, \quad k \in \mathbb{Z}, \tag{1}$$

where $\{j_1, \dots, j_N\}$ is any system of representatives modulo N.

Let us note two things: first, that indeed the sum does not depend on the choice of the system of representatives and second, that the sequence $\mathbf{c}$ thus defined is also N-periodic and it suffices therefore to know it in N indices forming a system of representatives modulo N. Both facts are due to the periodicity of the exponentials. Now, the orthogonality of the exponentials proves the following result.

Theorem 2.1.3. *The discrete Fourier transform N $\mathbf{b} \longrightarrow \mathbf{c}$ is a bijection in the set of N-periodic complex sequences. Moreover, the inverse application —* ***discrete inverse Fourier transform*** *— is the application given by*

$$b_k = \frac{1}{N} \sum_{n=0}^{N-1} c_n e^{2\pi i n \frac{k}{N}} = \frac{1}{N} \sum_{n=1}^{N} c_{j_n} e^{2\pi i j_n \frac{k}{N}}, \quad k \in \mathbb{Z} \tag{2}$$

with $\{j_1, \dots, j_N\}$ any system of representatives modulo N.

Due to the definition based on sequences, the discrete Fourier transform has also a clear continuity property.

In practice, it is very simple in any calculation program to perform these operations which are only addition and multiplication. However, the following problem arises: if N is very large, many operations need to be performed; so many, that most of the results could not be computed. Since most applications require dealing with a large amount of data, this problem was solved with the appearance of the Fast Fourier transform.

2.1.1 The Fast Fourier Transform algorithm

It was thanks to J.W. Cooley and J.W. Tukey, who designed in 1965 the Fast Fourier Transform (FFT) algorithm, that the number of operations was reduced significantly and Fourier theory could be applied to signal processing. In fact, Matlab performs the discrete Fourier

Transform via the Fast Fourier Transform with the command **fft**, hence the interest in this algorithm.

Let us examine this more carefully by estimating the number of operations that have to be performed, as a function of N, to compute a Fourier Transform. Let us set $N = \mathbb{N}$ and data $b_0, b_1, \ldots, b_{N-1}$. How many additions and multiplications must be computed to obtain the c_k coefficients? If we denote $\omega_N = e^{-2\pi i/N}$, $N-2$ multiplications need to be done to have all the N-th roots of unity (thus all the exponentials involved have been calculated, although in disorder). Then, for each coefficient c_k, N multiplications have to be done and to find the sum of N summands we have to do $N-1$ additions. Note that this is the maximum number of operations, according to the zeros that we had we could save many. Then, we can conclude that calling $\mathrm{oper}(N)$ to the total number of operations required for the calculation of all the coefficients c_k:

$$\mathrm{oper}(N) \leq (N-2) + N(N + N - 1) = 2N^2 - 2 = O(N^2). \tag{3}$$

In this context arose the FFT algorithm, to try to reduce this amount. The algorithm is based on the following idea: let us call $\mathbf{b} = (b_0, b_1, \ldots, b_{N-1})$ and change the c_j in the notation by $c_j^N(\mathbf{b})$ to express the dependence of N and $\mathbf{b}$. If N is even, i.e., $N = 2M$, we decompose the vector $\mathbf{b}$ of length $2M$ into two vectors, those of even coordinates and those of odd coordinates, and denote them b_0 and b_1, respectively. The crucial point is that $\omega_M = \omega_{2M}^2$ (due to basic properties of the exponential), since we can then write, for each j between 0 and $2M-1$:

$$\begin{aligned} c_j^{2M}(\mathbf{b}) = \sum_{n=0}^{2M-1} b_n \omega_{2M}^{jn} &= \left(\sum_{l=0}^{M-1} b_{2l}\omega_{2M}^{2jl} + \sum_{m=0}^{M-1} b_{2m+1}\omega_{2M}^{j(2m+1)} \right) \\ &= \left(\sum_{l=0}^{M-1} b_{2l}\omega_M^{jl} + \omega_{2M} \sum_{m=0}^{M-1} b_{2m+1}\omega_M^{jm} \right). \end{aligned}$$

That is, we proved that:

$$c_j^{2M}(\mathbf{b}) = c_j^M(\mathbf{b_0}) + c_j^M(\mathbf{b_1}) \cdot \omega_{2M}^j \quad j = 0, \ldots, 2M-1 \tag{4}$$

Notice that we considered that when j exceeds M:

$$c_j^M(\mathbf{b_0}) = c_{j-M}^M(\mathbf{b_0}), \quad c_j^M(\mathbf{b_1}) = c_{j-M}^M(\mathbf{b_1}), \tag{5}$$

using the periodicity of the discrete Fourier transform.

Let us now see how many operations (at most) are needed to calculate $c_j^{2M}(\mathbf{b})$ using this new expression. To compute the coefficients for the vectors $\mathbf{b_0}$ and $\mathbf{b_1}$, we need $2 \times \mathrm{oper}(M)$. Moreover, for the exponentials ω_M^j, $j = 1, \ldots, 2M$, we need $2M$ operations and to find each $c_j^{2M}(\mathbf{b})$, one multiplication and one addition. That is, for all of them, we need $2 \times 2M = 4M$ operations. Thus, we conclude that

$$\mathrm{oper}(2M) \leq 2\mathrm{oper}(M) + 6M, \quad \forall M \in \mathbb{N}. \tag{6}$$

In particular, this procedure will be optimal when N is a power of 2, as the data vector $\mathbf{b}$ can be subdivided into blocks of two until we reach 2, obtaining then the following result:

Proposition 2.1.4. *If* $N = 2^p$ *with* $p \in \mathbb{N}$*, then*

$$oper(N) \leq 4 \cdot 2^p p = 4N \log_2(N),$$

which gives

$$oper(N) = O(N \log N).$$

Proof. We will prove it by induction on p. For $p = 1$, we only have two coefficients, and it is easy to see that only 4 operations are needed, which is less than 6. Assuming the bound is true for p, using (6), we have:

$$\begin{aligned} \operatorname{oper}(2^{p+1}) &\leq 2\operatorname{oper}(2^p) + 6 \cdot 2^p \overbrace{\leq}^{(*)} 2\operatorname{oper}(2^p) + 8 \cdot 2^p \leq \\ &\leq 2 \times 4 \cdot 2^p p + 8 \cdot 2^p = 4 \cdot 2^{p+1}(p+1) = 4 \cdot 2^{p+1} \log_2(2^{p+1}) \end{aligned}$$

Where the inequality in (*) simply adds the operations due to a normalization factor to consider the maximum number of possible operations. ☐

Note that the reduction of operations is drastic. In particular, for $p = 10, N = 2^{10} = 1024$, as will be our case, the number of operations drops from about one million operations ($N^2 + N$) to only 40 000. That is, the proportion of operations we do less of increases exponentially with p.

2.2 Addressing the uniqueness of the phase problem: constraints

Sampling is the process of converting a signal into a sequence of values. Ever since this concept appeared in communication science, setting the rate at which the signal is univocally determined and distortion is avoided, has always been one of the main limitations in the field. Shannon laid the basis of this theory formulating the following theorem [6]:

Theorem 2.2.1. *If a function* $f(t)$ *contains no frequencies higher than* W *Hz, it is completely determined by giving its ordinates at a series of points spaced* $1/2W$ *seconds apart.*

This is commonly referred to as the Nyquist-Shannon theorem, where the threshold $2W$ is called the Nyquist rate. That is, at least twice the frequency of the sample needs to be measured in order to be able to retrieve the function correctly.

A few years later, Sayre, inspired by Shannon's sampling theorem, laid the groundwork for diffractive imaging in a half-page paper [7] . In it, Sayre sets out the sampling requirements in a crystallographic environment to directly reconstruct electron density from intensity measurements alone, making similarities of a periodic function with a crystal. Both works led to the development of the CDI theory as we know it today, which is explained below.

Given the density of an object $f(\vec{x})$, its Fourier transform $F(\vec{k})$ is given by:

$$F(\vec{k}) = \int_{-\infty}^{\infty} f(\vec{x}) exp(-2\pi i \vec{k} \cdot \vec{x}) d\vec{x} \tag{7}$$

where $\vec{x} = (x_1, x_2, x_3)$, the spatial coordinates in real space, and $\vec{k} = (k_1, k_2, k_3)$, the spatial-frequency coordinates in Fourier space. In practice, we approximate the object ($\vec{x}$) and the Fourier space ($\vec{k}$) by arrays. That is, we discretize the FT by using the conventional sampling, getting:

$$F(\vec{k}) = \sum_{\vec{x}=0}^{N-1} f(\vec{x}) exp(-2\pi i \vec{k} \cdot \vec{x}/N) \tag{8}$$

where $\vec{x}$ and $\vec{k}$ stand for pixels that range in each dimension from 0 to $N-1$.

Moreover, the Fourier Transform (FT) not only connects the object and its associated diffraction pattern, but also the real space itself with the reciprocal space. The spatial resolution in reciprocal space (δk) is obtained from the size of the reticle in direct space (D). What is more, the size of the reticle in reciprocal space (D_{rep}) is related to the resolution in direct space (δx), as defined in Equations (9) and (10), the so called reciprocal relationships.

$$\delta k = \frac{2\pi}{D} \tag{9}$$

$$D_{rep} = \frac{2\pi}{\delta x} \tag{10}$$

Therefore, increasing the size of the reticle in direct space (D) implies decreasing the pixel size in reciprocal space ($\frac{2\pi}{D}$); that is, improving spatial resolution in frequency space. Likewise, decreasing the pixel size in direct space (δx) we increase the reticle size in reciprocal space ($\frac{2\pi}{\delta x}$). Or in other words, improving the spatial resolution in real space requires to increase the reticle size (equivalent to the rocking curve size) in reciprocal space.

As introduced before, only the intensity -represented by the magnitude of the Fourier transform- can be experimentally measured, so the data taken correspond to the following set of equations:

$$I = \left|F(\vec{k})\right|^2 = \left|\sum_{\vec{x}=0}^{N-1} f(\vec{x}) exp(-2\pi i \vec{k} \cdot \vec{x}/N)\right|^2 \tag{11}$$

Hence, the phase problem consists in finding the modulus and the phase for $f(\vec{x})$ at each pixel.

We will then discuss Equation (11) under two conditions [9]:

- First, we assume that $f(\vec{x})$ is complex valued, which is its proper form. For a 1D object the total number of equations is N, but the total number of unknown variables is $2N$, since each pixel has real and imaginary part. For 2D and 3D, the total number of equations is N^2 and N^3, and the total number of unknown variables is $2N^2$ and $2N^3$, respectively.
- Second, we consider $f(\vec{x})$ real, which is how we are able to measure, and therefore determine it at first. According to Friedel's law[1] , the magnitude of its Fourier transform, $\left|F(\vec{k})\right|$, has central symmetry. Therefore, for a 1D real object, the number of equations reduces to N/2, while the number of unknown variables remains N. In the case of 2D and 3D real objects, the total number of equations becomes $N^2/2$ and $N^3/2$, respectively, with the total number of unknown variables being N^2 and N^3 in each case.

Based on the above analysis, it is suggested that, given the magnitude of a Fourier transform, the phase problem is underdetermined by a factor of 2 for 1D, 2D, and 3D objects, instead of factors of 4 and 8 for 2D and 3D objects, as one might think at first. This issue compromises the uniqueness of the solution to Equation (11) which is produced by the algorithm. Thus, in order to solve the phase problem, a necessary condition is that the number of unknowns and the number of equations must be equal. To achieve so, some constraints need to be introduced to simplify the problem, that will be described mathematically. Constraints can be applied in both real and reciprocal space, as will be detailed.

---

[1] Friedel's law is a property of Fourier transforms of real functions that states that given a real function $f(\vec{x})$, its Fourier transform $F(\vec{k})$ has the following property: $F(\vec{k}) = F^*(-\vec{k})$, that is: $|F(\vec{k})| = |F(-\vec{k})|$, which means that Bragg reflections related by inversion through the origin have equal amplitude.

Constraints in reciprocal space

To determine the necessary number of known pixels with in $f(\vec{x})$ to solve Equation (11), we define the concept of sampling ratio σ as follows [9]:

$$\sigma = \frac{\text{total pixel number}}{\text{unknown valued-pixel number}} \tag{12}$$

where the unknown-valued pixels are to be solved for.

Since the phase problem is under-determined by a factor of 2, the equations should have a unique solution as long as $\sigma > 2$, as was introduced above. Hence the strategy to increase the number of the number of equations (the total number of pixels) is to use the oversampling method. This technique involves sampling the magnitude of the FT (in the reciprocal space) finely enough to ensure $\sigma > 2$.

Particularizing for a square object, as in our case or study, in each dimension, the oversampling condition is expressed as:

$$\sigma > 2^{1/n} \tag{13}$$

where n is the total number of dimensions. This requirement corresponds to the oversampling by $\sigma > 2$ for a 1D object, $\sigma > 2^{1/2}$ in each dimension for a 2D object, and $\sigma > 2^{1/3}$ in each dimension for a 3D object. Interestingly, the oversampling requirement per dimension is lower for 3D objects compared to 2D objects. It has been demonstrated that for 1D signals, no unique solution to the problem of recovering a signal from the amplitude of its Fourier transform exists [5, 10].

Therefore, to maintain an oversampling ratio of $\sigma > 2$ we should ensure that in the reciprocal space there are at least 2 detector pixels (δk) across the width of each intensity fringe (Δk) in the diffraction pattern measured:

$$\frac{\Delta k}{\delta k} \geq 2 \tag{14}$$

Constraints in real space

This case correspond to constraints applied on the object itself. In particular, the zero-padding and the positivity constraint will be explained [9]. These have a particularly important role in the case of loose supports. That is, supports larger than the real size of the object, that need to be updated upon the iterations of the algorithm, to adjust eventually to the object.

The first approach to be examined is to decrease the number of unknown variables by using objects that contain some pixels with known values, in particular zero valued. This consists in padding the object distribution (unknown-valued pixels) with known valued pixels (as zeropadding) in the object domain, automatically leading to oversampling of the signal spectrum in the Fourier domain, which is the main goal.

Secondly, although each equation in the set presents two possible solutions due to the modulus, the positivity constraint remove one of the two, as explained below. For complex-valued objects, as occurs in the case of X-ray diffraction, the complex-valued object intensity can be expressed by $\rho = A \cdot e^{i\phi}$, where the amplitude A is related to the electronic density (typically $A > 0$), and the phase ϕ contains information about structural distortions in the crystalline lattice (always positive for ordinary matter). Consequently, it has been proposed that the positivity constraints on the imaginary part of complex-valued objects can generally be employed as internal constraints for phase retrieval. That is, for X-ray diffraction, our field of interest, it is sufficient to select the positive solution of Equation (11) and disregard the negative one.

2.3 Algorithms: a description

A coherent beam implies a FT between real and reciprocal space. Based on the FT and its inverse, we have two fundamental tools to move between the object ρ in real space and the diffracted field Ψ in the reciprocal space:

- Forward problem: $\Psi = F[\rho]$
- Inverse problem: $\rho = F^{-1}[\Psi]$

where F stands for the FT operator.

A particularly successful approach to solving these problems is the use of optimization algorithms which seek for the object ρ which minimizes an error metric defined as:

$$\epsilon^2 = \sum \left(\sqrt{I_{exp}} - |\Psi| \right)^2 , \tag{15}$$

where I_{exp} is the set of experimental diffraction patterns measured in the rocking curve and $|\Psi|$ is the modulus of the diffracted wavefield calculated from the guessed ρ.

These are iterative tools that begin with an initial guess of the optimal values of the variables and generate a sequence of improved estimates until they reach the global minimum of ϵ^2, compatible with the level of noise with which the experimental data have been measured. The strategy used to move from one iterate to the next is what distinguishes one algorithm from another. In our case, algorithms involve iterative Fourier transformation back and forth between the object and Fourier domains and the application of aforementioned constraints in each domain. There are various sorting strategies to update the object during the algorithm iterations, such as Error reduction [11], Hybrid-Input-Output [11] and Shrink-Wrap [12], as will be described .

Error reduction (ER)

The Gerchberg-Saxton algorithm was originally invented in connection with the problem of reconstructing the phase from two intensity measurements acquired in two different planes. Typically, the two planes are the image plane and the diffraction plane, and the wavefront propagation between these two planes is given by the Fourier Transform. However, in CDI, only one intensity measurement is available – the diffraction pattern, and some *a priori* information about the object distribution is known. Exploiting these facts, the algorithm consists of the four simple steps detailed in the scheme in Figure 3.

In this approach, the method simply transforms back and forth between the two domains, ensuring that constraints are met in one domain before returning to the other. This adaptation of the Gerchberg-Saxton algorithm is known as the Error-Reduction (ER) algorithm, as the error (as defined in (15)) decreases with each iteration, it can only be the same or less than the error at the previous iteration. The process repeats until the computed FT fulfills the Fourier-domain constraints, or the generated image meets the object-domain constraints.

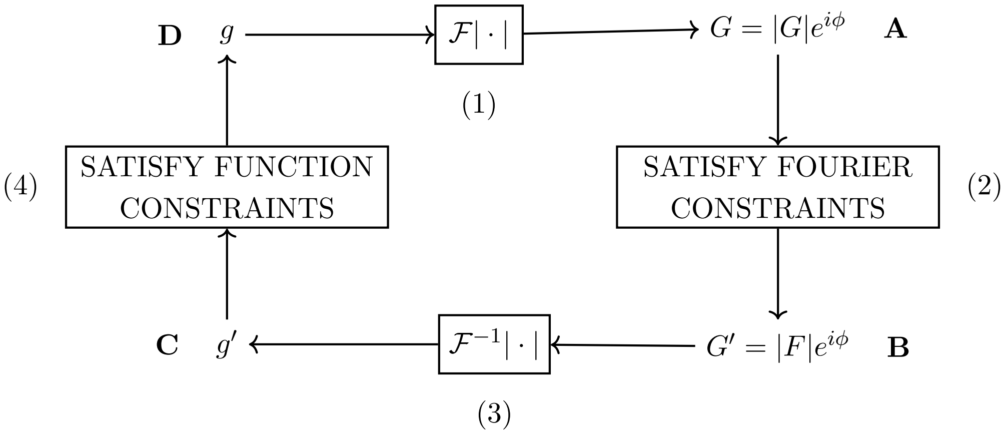

Figure 3: *Block diagram of the ER (Gerchberg-Saxton) algorithm, containing the following four steps: (1) Fourier transform an estimate of the object, (2) replace the modulus of the resulting computed FT with the measured Fourier modulus to form an estimate of the FT, (3) inverse Fourier transform the estimate of the FT and (4) replace the modulus of the resulting computed image with the measured object modulus to form a new estimate of the object satisfying the object-domain constraints. The letters* ***A***, ***B***, ***C*** *and* ***D*** *denote the results after steps (1), (2), (3) and (4), respectively. Adapted from [11].*

That is, the fourth step of the ER algorithm reduces to Equation (16):

$$g_{k+1}(x) = \begin{cases} g'_k(x), & x \notin \gamma, \\ 0, & x \in \gamma, \end{cases} \tag{16}$$

where γ is the set of points at which $g'_k(x)$ violates the object-domain constraints.

At this point, the solution —a Fourier transform pair that meets constraints in both domains— is achieved. Convergence is typically monitored by evaluating ϵ^2 (see Eq. 15).

A notable limitation of this algorithm, however, is its relatively slow convergence. While error reduction is significant over the initial thirty iterations, it then slows considerably, approaching a plateau with minimal additional decrease. Moreover, another important limitation is the stagnation in local minima, this is why HIO had been introduced.

Hybrid-Input-Output (HIO)

A solution to the problem of the slow convergence of the ER algorithm has been the Input-Output (IO) algorithm, which has proved to converge faster for the problem of one intensity measurement. The IO algorithm differs from the ER algorithm only in the object-domain operation. The first three operations are the same for both algorithms -as can be seen in the algorithm scheme in Figure 4-, which can be thought of as a nonlinear system having an input $g(x)$ and an output $g'(x)$. A key property of this system is that its output always produces an image with a Fourier transform satisfying the required Fourier-domain constraints.

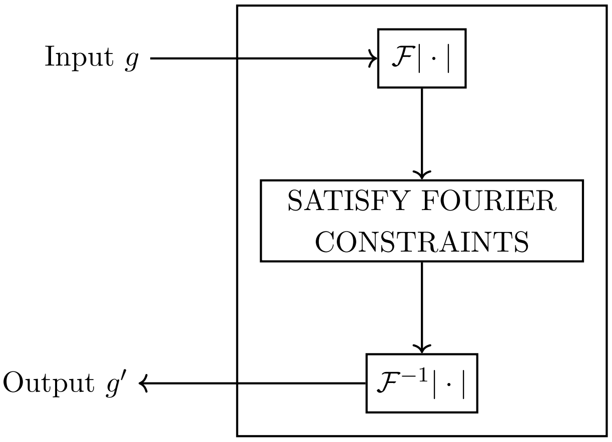

Figure 4: *Block diagram of the system for the HIO concept, containing the following steps. The first three operations are the same as in the ER algorithm: Fourier transforming the object $g(x)$, satisfying the Fourier-domain constraints and inverse Fourier transforming the result to get $g'(x)$. However, in this case, the input $g(x)$ no longer must be thought of as the current best estimate of the object, but as the driving function for the next output $g'(x)$, which provides some freedom in defining an algorithm that converges more rapidly to the solution. Adapted from [11].*

In the IO algorithms, the input for the next iteration $g(x)$ does not necessarily satisfy the object-domain constraints. This idea provides substantial flexibility in choosing the subsequent input, paving the way for developing algorithms that converge more rapidly to a solution. In particular, even though the IO algorithm is actually a class of algorithms, we will focus on the Hybrid-Input-Output (HIO) algorithms, described as follows:

$$g_{k+1}(x) = \begin{cases} g'_k(x), & x \notin \gamma, \\ g_k(x) - \beta g'_k(x), & x \in \gamma, \end{cases} \tag{17}$$

where γ is defined as in (16) and the feedback parameter β is a constant to be determined to damp the application of the support constraint. Feedback allows for the pixels to be updated both within and outside the support (in a certain range). This prevents the algorithm from getting trapped in a local minimum of the error metric. Typically, $\beta = 0.9$ is selected.

In this algorithm, we exploit the above mentioned property of the nonlinear system that if an output g' is used as an input, its output will be itself, since the FT of g' already satisfies the Fourier-domain constraints. On the other hand, where the constraints are violated, the desired change of the output, in order for it to satisfy the object-domain constraints, is one that drives it to a value of zero, and therefore, the negative of the output at those points.

Shrink-Wrap

The Shrink-Wrap (SW) algorithm is a further modification of the ER algorithm, periodically updating the object support in step (4) -Figure 3- during the iterative reconstruction process at each 20-th iteration. Over time, this adjustment enables the object support to closely match the true shape of the object distribution, ultimately achieving a “tight support”.

The innovation proposed is the simple but powerful use of the current estimate of the object to determine the support constraint. Through the standard process of the ER algorithm, this refined support constraint further enhances the object estimate. What is more, we find that this method is very stable and converges to the correct support and object for both simulated and experimental X-ray-diffraction data.

2.4 Limitations of standard algorithms and how to address them

As was introduced in Section 1 when the rocking curve was defined, there is one common assumption in all these algorithms, which is that the objects are static in the time frame over which an individual rocking curve is measured.

However, when measuring experimentally in the laboratory, it is common to have a non-regular sampling of the intensity (the sampling in the rocking curve direction is not performed over a regular angular grid) or a non-static object (objects whose morphology or internal structure change during the rocking curve measurement).

These situations can occur, for example, when a stationary incident beam illuminates a sample undergoing uncontrolled rotation (as in high-temperature experiments) or imprecise experimental stages, difficult-to-stabilize sample environments or, even, to the torque exerted by the x-ray beam on the sample (the so called radiation pressure). All these non-expected processes lead to a detrimental effect of the angular positioning error of the sample. However, they only will be noticeable when they are at levels commensurate with goniometer uncertainties, that is, the angular resolution we are able to measure experimentally.

To address these challenges we need to change the implementation of the Fourier Transform at the core of the reconstruction algorithm. This is to substitute the 3D FT by a series of 2D FT as done in the Fourier Slice Theorem.

2.4.1 The Fourier Slice Theorem

The Fourier Slice Theorem (also known as the Fourier Projection-Slice Theorem), discovered by Bracewell in the context of radio astronomy [13] is formulated in its classical version as follows [14]:

Theorem 2.4.1. (Projection-Slice Theorem) *Let $F(u,v)$ be the Fourier Transform of the function $f(x,y)$. Then, the Fourier Transform of the projection of $f(x,y)$ in the direction θ is equal to the slice through $F(u,v)$ in the corresponding direction.*

This theorem thus states that a 1D slice of a 2D function's Fourier spectrum is the Fourier transform of the projection of the 2D function, and is the theoretical foundation of many medical imaging techniques. Conceptually, the theorem works because the value at the origin of frequency space gives the integrated value of the signal, and rotations do not fundamentally change this fact. The theorem works for jittering and shearing operations as well as rotations, since shearing a space is equivalent to rotating and dilating the space. From this perspective, it makes sense that the theorem generalizes to higher dimensions. In particular, throughout this work the projection in 2D of a 3D function will be employed.

3 Reconstruction of an ideal cubic crystal using standard algorithms

As a first result and approximation to reality, we implemented an algorithm based on the ones described in Section 2. To test the performance of the algorithm and study its convergence behavior, an ideally static three dimensional crystal was simulated, its corresponding 3D diffraction pattern was calculated and inverted with that algorithm. Section 3.1 describes how the crystal was created together with its associate 3D diffraction pattern and Section 3.2 describes the algorithm and its implementation.

3.1 Code to simulate the cubic crystal

The simulation of the crystal was performed using MATLAB and own functions [15]. The chosen space was a cube of side 128 pixels, in which the cubic crystal ρ was defined. Note that a power of 2 has been chosen as the array size, given the importance of what was above explained in Section 2.1.1 regarding the FFT algorithm.

While the whole space was defined as a grid of zeros of the mentioned size, a cubical grid of side 21 pixels with ones was defined in its center, as is presented in Figure 5a, representing the ideal crystal. Moreover, Figure 5b shows the diffraction pattern associated with the cube. That is, the intensity that would be measured from that sample, and the only data we have available to process and retrieve the amplitude and the phase of the signal in the original sample. This diffraction pattern, as was previously explained in Section 2, was computed by performing the Fourier transform to the simulated data and obtaining its square modulus, $|F(\rho)|^2$. As a result, note that the maxima in real space, with a value of 1, correspond to a value of 2π in the reciprocal space. We refer to this simulation as “ideal” since neither Poisson noise nor rotations or undesirable defects in the measurements are being introduced.

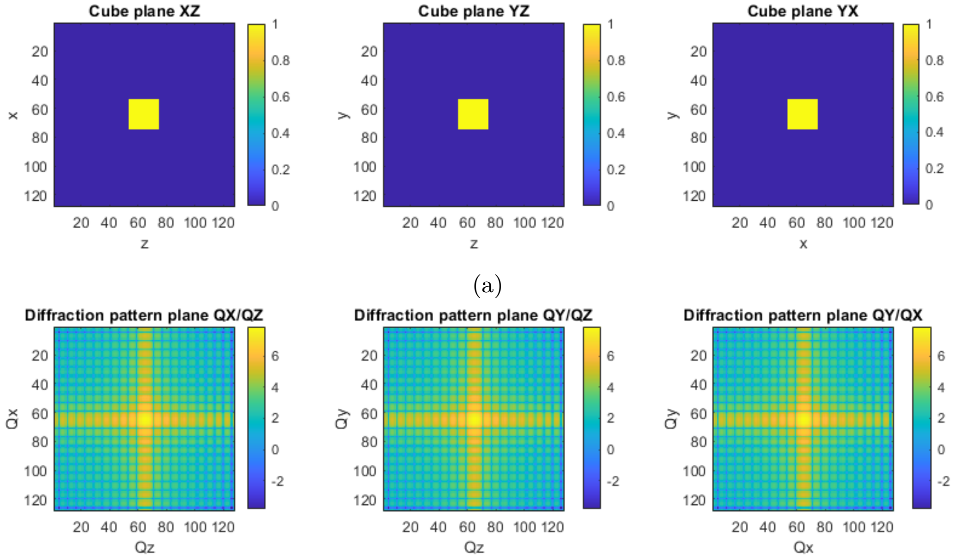

(a)

(b)

Figure 5: *Simulated cubic grid of 128 pixels with a 3D cubic crystal of 21 pixels of side in its center. Views of the three main planes in (a) the real space and (b) the reciprocal space.*

3.2 Implementation of the proposed algorithm

As was introduced in Section 2, although many phase retrieval algorithms have been developed, the two most commonly used are the ER and HIO algorithms. The most common practice for CDI phase retrieval is to alternate between both, while periodically updating the support via the SW method. In this work we will also make use of this combination, based on the one implemented in reference [15]. In addition, the evolution of the error metric (see Eq. 15) is monitored over the course of the iterations, since it is the parameter which quantifies the degree of congruence between the retrieved object and its diffraction pattern and the experimental measurements. In definitive, it quantifies the convergence behavior of the algorithm and establishes a number of iterations beyond which the reconstruction won't be improved. This happens when the error metric has reached its global minimum.

The algorithm consists in a total of 560 iterations, organized as shown in Table 1. These include five cycles of ER + HIO, in which the support is updated in the middle of each ER sequence via SW, ending with 200 ER iterations to ensure the error metric reaches its lowest point. Nevertheless, the exact number of iterations was fixed experimentally, by performing numerous tests and observing the evolution of the results for the different cases.

ER	20-SW-20	20-SW-20	20-SW-20	20-SW-20	20-SW-20	200
HIO	20	20	20	50	50	

Table 1: *Iteration steps for the combined algorithm, consisting of five cycles of ER-HIO and 200 ER iterations at the end. Note that in the middle of every ER series the support is updated via SW.*

As explained in Section 2.3, the ER algorithm is most efficient during its first 20–30 iterations, which is why it is used sparingly. Additionally, as detailed for the SW, it is applied every 20th ER iteration, hence the chosen cycle structure. Regarding the HIO algorithm, while it temporarily increases the error metric, it produces a better object estimate, allowing for the subsequent ER series to reduce the error metric more effectively. The number of iterations also increases in the final two cycles. Observing the progression of the error metric (like the one presented in Figure 6), it becomes evident that as the error metric decreases, the HIO algorithm requires more iterations to stabilize. Finally, the algorithm concludes with a series of 200 ER iterations. Although the most significant reduction in the error metric occurs during the first 20 iterations, improvements continue steadily throughout the entire series.

Since there is a noticeable variability in the quality of the final reconstruction, we followed the procedure used in [16]: we repeated the ER/HIO/SW cycle 10 times and we chose the reconstructed object and the support yielding the lowest error metric as the final reconstruction. This error metric is presented in Figure 6, in which the different stages of the algorithm have been pointed out. The final error metric ϵ^2 obtained was 0.138, as seen in the graph.

Although it is not the minimum error metric that can be obtained with this type of algorithm, we can be satisfied with the result, given the initial point. Starting from a better estimation of the object (and thus a lower value of the error metric), the algorithm would be able to decrease the minimum value of the error metric much more, as expected. Notice also that given our object and the initial conditions that are provided, increasing the number of iterations does not lead to a better final result but to a probable stagnation in a local minimum, as was observed in several trials. Hence the reason of the “low” number of iterations in the whole algorithm, since computational time in this case was not an issue, the algorithm did not take more than a few minutes to proceed.

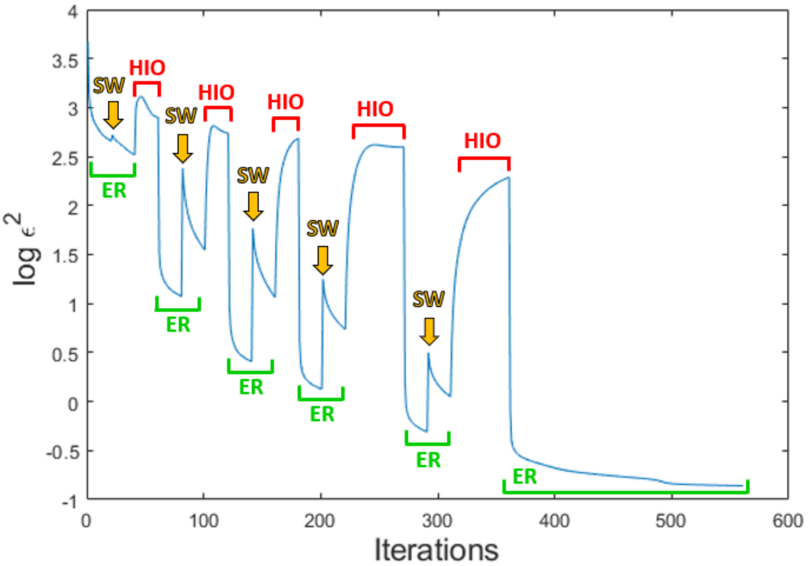

Figure 6: *Evolution of the error metric over the cycles of standard ER/HIO/SW algorithms. The error metric achieved after the 560 iterations was* $\epsilon^2 = 0.138$.

As emphasized in the previous sections, our final goal is to recover the amplitude and phase of the sample that is being measured. Since the last step of the algorithm is a series of ER iterations (Table 1), the evolution throughout the last iteration was displayed in order to show the effect of the algorithm, as well as the reached final result. Recalling the scheme of the ER algorithm presented in Figure 3, the results **A**, **B**, **C** and **D** after each of the steps were plotted. The result is presented in Figure 7 and it shows all the features of the algorithm aforementioned in Section 2.3, allowing for a deep understanding and summarizing the effect of the algorithm in a very clear way, showing the outcome in the final result. Taking advantage of the cubic symmetry of the system, only one of the three planes is presented as the amplitude of the system.

Before explaining all the phases in detail, it is worth noting that steps **A** and **B** belong to the reciprocal space, thus they have a diffraction pattern in the amplitude map. On the other hand, **C** and **D** belong to the real space, so the amplitude in this case in fact matches the shape of the object. In the first row, **A** is displayed, obtained by applying a FT to the object obtained from the previous iteration, thus it is complex. Since we are only measuring the intensity, the diffraction pattern on its right consists of a distribution around the Bragg peak, where the phase remains a random grid between $-\pi$ and π.

In the following step of the algorithm, Fourier constraints are applied, so in **B** the amplitude is updated, whereas the phase remains as before.

Subsequently, an inverse FT is applied to the estimate of the object and **C** is obtained. In the first plot of the third row, both the support (in the yellow shadow) and **C** (in green) are plotted, where it can be appreciated the slightly different sizes of both. The plot next to it depicts the support, a grid full of zeroes with a cube in its center that clearly shows the goal of this tool, a binary filter to delimit the size of the object. With respect to the angle of **C**, although it is still not well defined due to the phase problem (the phase is not unique after only applying an inverse FT), the cubic shape of the object is already distinguishable.

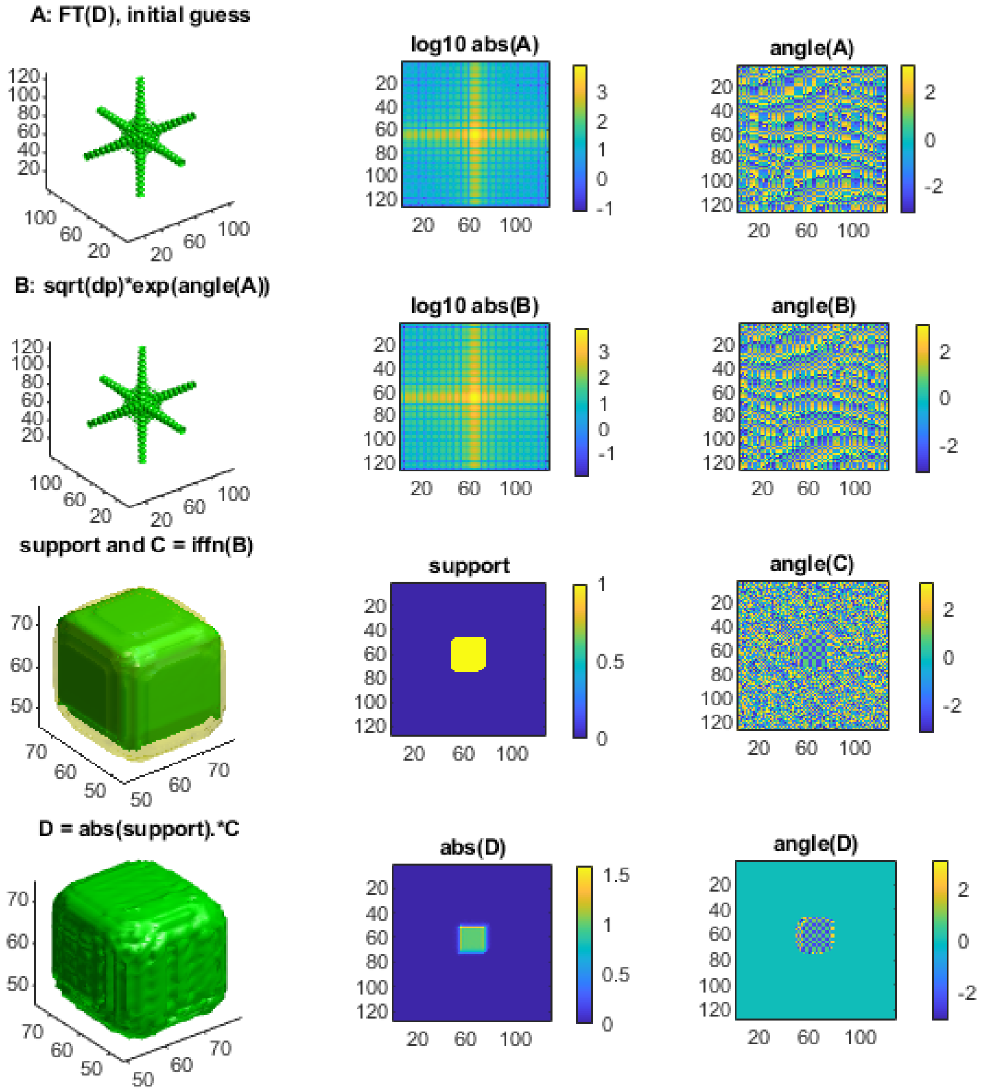

Figure 7: *Evolution of the amplitude (shown as abs(·)) and the phase (angle(·)) of the reconstructed object and diffraction pattern throughout the last iteration of the ER algorithm series. The results* ***A****,* ***B****,* ***C*** *and* ***D****, defined as in Figure 3 are plotted. Note that steps* ***A*** *and* ***B*** *belong to the reciprocal space, thus the Bragg peak in the amplitude map. On the other hand,* ***C*** *and* ***D*** *belong to the real space, so the amplitude in fact matches the cubic shape of the original object that we are trying to reconstruct.*

Lastly, after applying the function constraints using the support, the final object is recovered. The shape of **D** now matches the one of **C** but having expanded it to cover the whole support volume. With respect to the amplitude, now it in fact matches the cubic original shape of the object we are trying to reconstruct: a grid full of zeroes, corresponding to the empty space, with a smaller cube in the center of amplitude one, as was defined initially. Regarding the phase, now it is also a grid full of zeroes, corresponding to the empty space, with a smaller cube in the center of a random grid between $-\pi$ and π, as was expected.

All in all, although the cube is not perfectly sharp at the edges, we can be more than satisfied with the obtained reconstruction of the object, given the limitations of the algorithm.

4 Reconstruction of a shear artifact using the Fourier Slice Theorem

Once we have evaluated the quality of the reconstruction on a simplified experiment (see previous section), we can evaluate the quality of the reconstruction in an experiment closer to reality. To simulate a more realistic experiment, we rotate the crystalline cube with respect to the incident angle direction in an angle θ. As we will see, the standard algorithm, based on a 3D FT, introduces systematically a shear artifact in the reconstructed object. To correct for this effect, we will propose a modification of the algorithm where we will substitute the 3D FT by a series of 2D FTs, according to the Fourier Slice Theorem. Finally, to push further the limits of the algorithm performance in realistic experiments, we will include an angular uncertainty (that we call *jitter*) to simulate uncontrolled rotations of the crystal during the measurements. By varying the degree of jittering (i.e. the level of angular perturbation), we will quantify the extent of artifacts introduced in the reconstruction during an experiment taken in realistic conditions (e.g. measurements of rocking curves during crystal annealing).

Section 4.1 describes how the crystal was created and what scattering geometry was adopted. Section 4.2 compares the effect of a 3D FT versus a series of 2D FT (Fourier Slice Theorem) on the inversion of this realistic rocking curve scan. Note that in this section we do not process the data through an algorithm, we only use the Fourier Transformation in different ways to observe the object which would be virtually obtained.

4.1 Code to simulate a realistic experiment

As performed above in Section 3.1, the simulation of the Bragg CDI experiment on a cubic crystal was carried out performed using MATLAB and own functions [15]. Once again, the chosen space was a cube of side 128 pixels, in which the cubic crystal ρ was defined. For the same reason as before (see Section 2.1.1), a power of 2 was chosen as the array size.

The whole space was defined as a grid of zeros of the mentioned size, whereas the crystal is represented in its center by a cubical grid of side 21 pixels. In this case, a rotation at an angle of $\theta = 26.7^\circ$ with respect to the incoming beam was introduced. This allows for capturing the Bragg reflection of crystalline planes which are perpendicular to the direction of the momentum transfer $\mathbf{Q}$, as seen in Figure 8. Then, we calculate the 3D diffracted intensity captured by the detector in a rocking curve scan where the angular step between cuts is $\delta\theta = 0.0156^\circ$, with a total of 256 cuts.

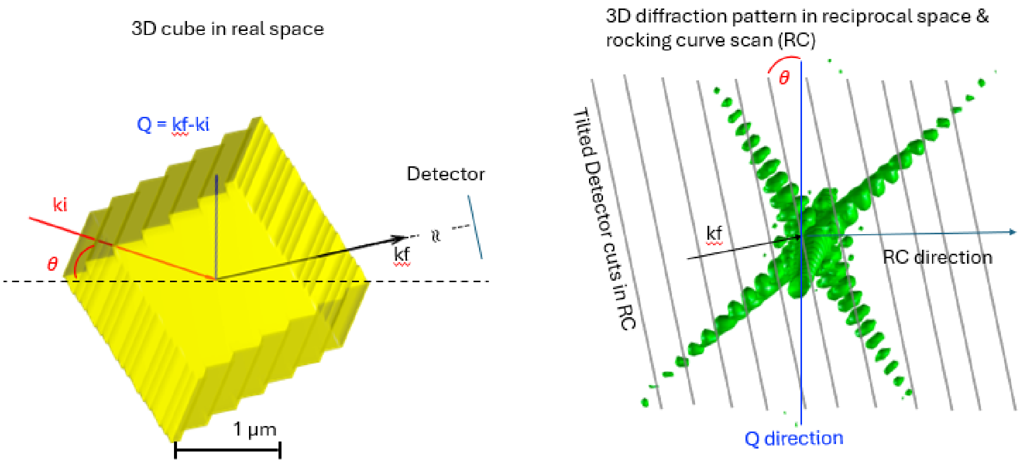

Figure 8: *On the left panel, simulated cubic crystal of 21 pixels of size (corresponding to* $2.1 \cdot 10^{-6}$ *m), rotated at an angle of* $\theta = 23.7°$ *with respect to the horizontal plane. On the right panel, associated 3D diffracted intensity distribution around the Bragg peak in reciprocal space, along with its rocking curve scan. Adapted from [4].*

Finally, Poisson noise was introduced in the diffraction patterns of the rocking curve in order to reproduce more accurately the detection process, which is in essence stochastic (see Figure 9). The major effect of the Poisson noise is the loss of information at high frequencies, which also affects at the spatial resolution with which we can reconstruct the object.

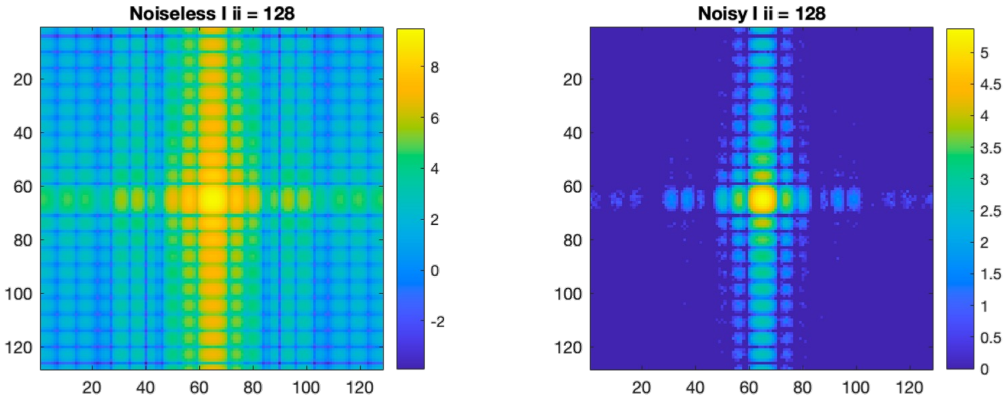

Figure 9: *Left panel: noiseless diffracted intensity slice registered by the detector when it cuts the center of the Bragg peak. Right panel: same cut but with Poisson noise, where a significant loss of information associated to high spatial frequencies is observed.*

4.2 Implementation of the Fourier Slice Theorem and correction of the shear artifact

In this case, to recover the original object, if we inverse Fourier transform with a 3D IFFT the diffracted wave field registered by the detector plane in the rocking curve, we observe that the resulting crystal is no longer cubic but has been distorted. In particular, it presents a shear of its shape, as seen in Figure 10. This shear is an artifact which arises from the tilting of the detector planes in the rocking curve scan with respect to the direction of the Q vector, which is not taken into account by the 3D IFFT.

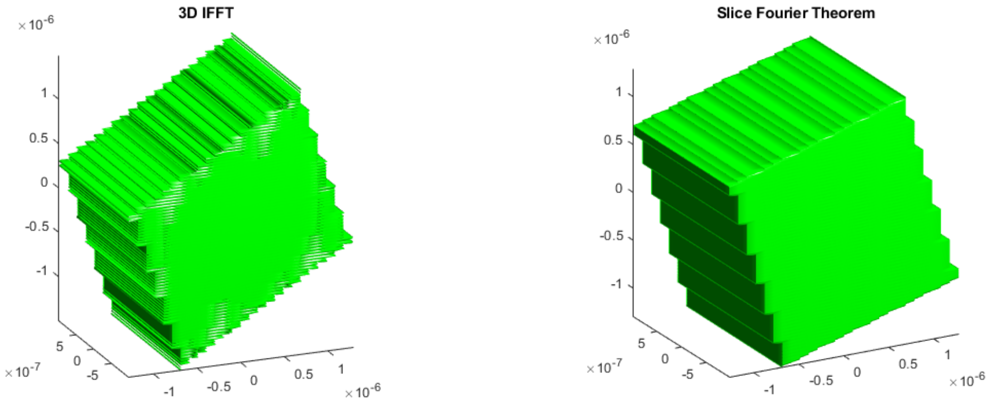

(a) (b)

Figure 10: *3D Inverse FT result of the rocking curve scan data set of the simulated rotated crystal, using (a) the 3D Inverse FFT and (b) the Slice Fourier Theorem.*

Thus, to avoid the introduction of this shear artifact we need to modify the forward problem by which we connect the direct and reciprocal space. This new forward model should describe explicitly the wave-field at each slice, Ψ_j. To achieve so, we will make use of the Fourier Slice Theorem, which enables to use a 2D Fourier transformation (F_{2D}) that acts on a 3D → 2D projection of the 3D object (ρ) modified by a multiplicative phase term as follows:

$$\Psi_j \equiv \Psi(\vec{q}, \vec{\Delta}_j, \rho) = F_{2D}\left\{R_z[Q(\vec{\Delta}_j)\rho]\right\} \tag{18}$$

where $\vec{q}$ stands for the momentum transfer vector, $\vec{\Delta}_j$ for the phase shift term, ρ for the 3D object, F_{2D} for the 2D Fourier Transform operator, R_z for the projection operator and $Q = exp(i\vec{\Delta}_j \cdot \vec{x})$ for the phase term. In this expression, the essential feature is the term Q, which allows for calculating slices of Ψ corresponding to a set of arbitrary incident angles that do not need to follow a regular pattern. This works because any given rotation of the sample away from the Bragg angle ($\Delta\theta_j$) can be represented as a corresponding shift of the detector's measurement plane by a vector $\vec{\Delta}_j$ in reciprocal space, moving away from the Bragg peak [15].

4.2.1 Effect of the angular uncertainty (jitter) in the quality of the reconstruction

In this last section, we will compare the reconstruction quality that would be potentially obtained if we were to use the standard algorithm versus the algorithm based on the new forward problem to invert the rocking curve data sets where angular jittering has been included. Thus, in this case we can't properly speak about *reconstruction* (which would imply the use of iterative algorithms) but simply about *inversions* of diffracted wave field by the means of Fourier Transform based operations.

Finally, the level of jittering is defined as a percentage of the angular step $\delta\theta$ which separates successive cuts in the rocking curve, and which in our case is of 0.0156°. By gradually changing that level, we model different degrees of instability of the object under realistic conditions.

The quality of the inversion was quantized via the cosine similarity. This metric measures the similarity between two vectors by calculating the cosine of the angle between them, namely:

$$cos(A, B) = \frac{A \cdot B}{\|A\| \cdot \|B\|} = \frac{\sum_i a_i \cdot b_i}{\sqrt{\sum_i a_i^2}\sqrt{\sum_i b_i^2}} \tag{19}$$

where A and B are the two vectors. Here, vector A stands for the original object and vector B is the inverted object.

Thus, this expression returns a value between -1 and 1, where a value closer to 1 indicates greater similarity between the original and the retrieved object (or equivalently, an angle of 0 between the two vectors). The results for different percentages of jittering are presented in Table 2.

% of jitter	**3D IFFT**	**2D Slice Fourier Theorem**	**Angular uncertainty (°)**
0	0.89275	1.00000	0
1	0.89254	0.99999	$1.56 \cdot 10^{-4}$
2	0.89265	0.99998	$3.12 \cdot 10^{-4}$
5	0.89392	0.99969	$7.80 \cdot 10^{-4}$
10	0.88861	0.99952	$1.56 \cdot 10^{-3}$

Table 2: *Cosine similarity between the original object and the retrieved one, via the 3D IFFT -first column- or the 2D Fourier Slice Theorem -second column-, and associated angular uncertainty -third column-, for different degrees of jitter in the rocking curve data.*

From the correlation results shown in the table above, one may think there is not much difference in the obtained results; nor between the 3D IFFT and the 2D Slice Fourier Theorem, nor among the different jittering percentages. However, if we plot the retrieved objects for all cases, the conclusions that can be drawn are significantly different. The 3D of the retrieved objects in all these cases are plotted in Figure 11.

In particular, the jittering was simulated to be 1, 2, 5 and 10% of the rocking curve scan data. Although the numerical difference in the correlation is very slight, the distortion can be clearly noticeable as the jitter increases. In this line, it should be remembered that the ultimate goal of this type of diffraction imaging is to recover the original object, not only to obtain a numerical similarity to it, thus the importance of representing the data.

Moreover, for a 10% of jitter, the original object, which is a solid cube, cannot even be recognized due to the high amount of artifacts that appear in the image. The Poisson noise introduced, together with the jitter, make it impossible to have enough useful data. However, this percentage of jittering is pretty high and probably not even realistic in an experimental setup, but it is useful to display the effect of the jittering when applying the Inverse Fourier Transform.

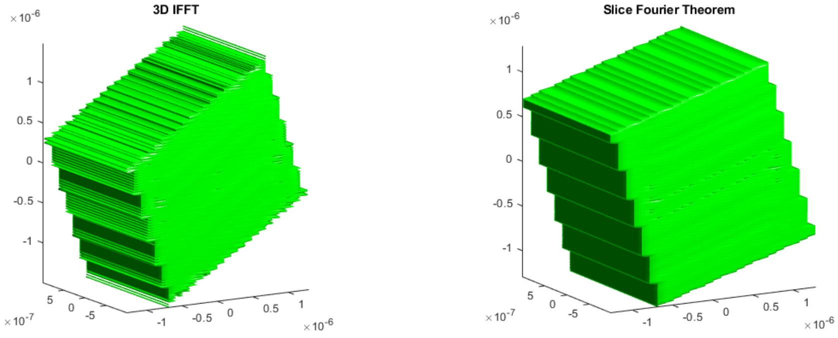

(a) *1% jitter.* (b) *1% jitter.*

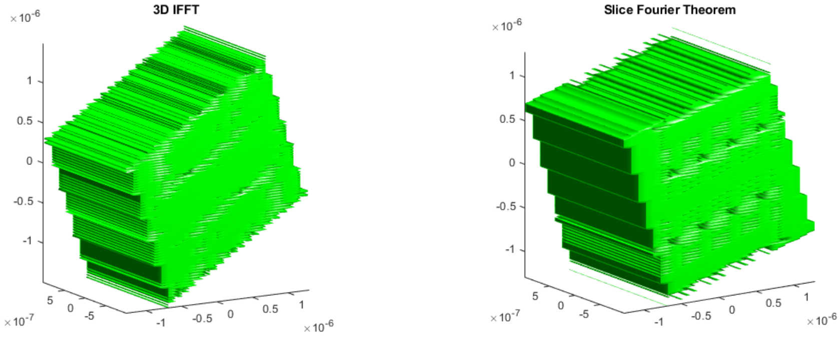

(c) *2% jitter.* (d) *2% jitter.*

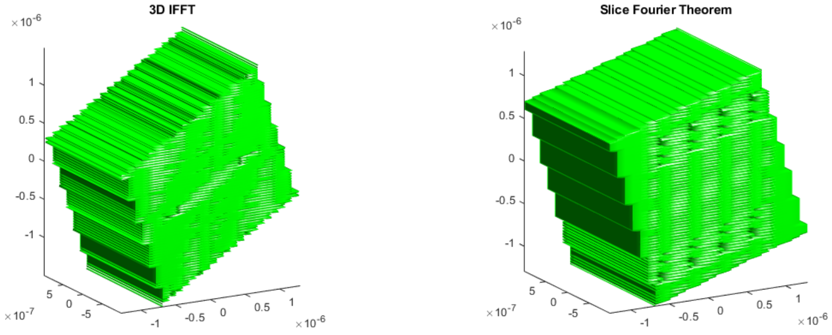

(e) *5% jitter.* (f) *5% jitter.*

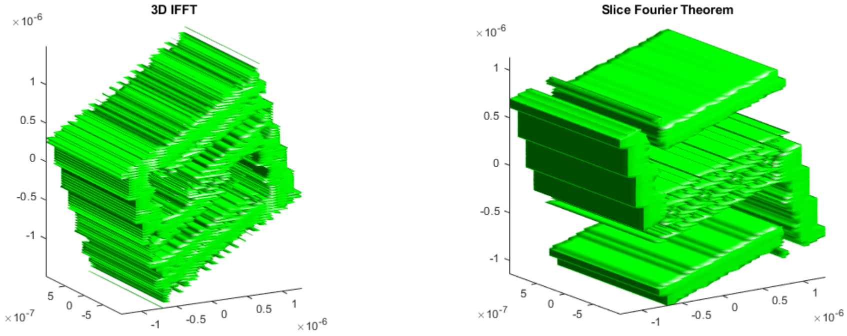

(g) *10% jitter.* (h) *10% jitter.*

Figure 11: *3D Inverse FT result of the rocking curve scan data set of the simulated rotated crystal, using the 3D Inverse FFT and the Slice Fourier Theorem, for a certain jitter percentage in the rockinng curve data.*

5 Conclusions

This work presents a study of numerical algorithms used for the reconstruction of crystalline objects measured with the microscopy technique: *Bragg Coherent Diffraction Imaging.* As we have explained these algorithms make use of the properties of the Fourier Transform to extract structural information from diffraction patterns measured in the reciprocal space arising from the scattering of a coherent X-ray beam by a crystalline sample.

Initially, the theoretical foundations of the (Discrete) Fourier Transform were presented and its weaknesses when implementing these operations in an algorithm, giving rise to the Fast Fourier Transform. Then, the mathematical definition of the FT was connected to the formalism used in Coherent Diffraction Imaging. In this line, it was explained how the the characteristics of the FT lead to the properties of both the real and diffracted fields, and the phase problem was addressed, detailing the constraints it requires. Subsequently, several well-known algorithms in phase retrieval were explained: Error-Reduction, Hybrid-Input-Output and Shrink-Wrap. However, these algorithms have a common denominator which is the static assumption of the object. Thus, whenever this condition is not met, this requires a new approach of the forward problem, solved by introducing the Fourier Slice Theorem. These new algorithm strategies have been explored in recent years and these are the ones that were examined in this work.

The first results of this work, show how an ideal crystal was simulated and recovered using standard algorithms. In particular, an algorithm was proposed combining cycles of the three aforementioned algorithms. An optimal series of iterations was obtained (Table 1), attending to the performance and limitations of each of the algorithms individually and thus, its impact on the evolution of the error metric. Moreover, the behavior of every step in the last iteration was shown in order to demonstrate the effect of the implemented algorithm and the object was retrieved successfully. However, there are some features in Figure 7 that are worth explaining. A phase ramp, in the form of a wavy pattern can be observed both in $angle(A)$ and $angle(B)$, which is most likely due to the reconstructed object being slightly displaced with respect to the center. Indeed, the cube was simulated rounding 1/6th of the total 128 pixels, that is, with a size of 21 pixels instead of 21.33. This slight difference is yet enough to create this artifact. Also, the high frequencies in $angle(D)$ (represented by the kind of checkerboard that appears) are also probably due to that effect.

Secondly, the performance of the algorithm was evaluated when applying the algorithm to an experiment closer to reality. In this case, the crystal was rotated with respect to the incident angle direction and an angular uncertainty (namely *jitter*) was introduced. To correct for the effect that the 3D FT introduces in this cases, a modification of the previous algorithm was proposed, based on the 2D Fourier Slice Theorem. This led to significant improvements in the quality of reconstruction, as was shown. However, the numerical correlation between the retrieved object and the original one was proved to be not enough to evaluate the goodness of the result and so the need of 3D plotting the final object was demonstrated. Nonetheless, as occurred before, a slight phase ramp can also be seen in the retrieved object, likely due to the same reason as above. Moreover, it should also be taken into account that although jitter can be corrected experimentally by trying to model the evolution of the sample over time, the Poisson noise is intrinsic to the process of detection. Thus, it has to be introduced in the reconstruction, even though it clearly worsens the results, being more noticeable in the cases of relatively high percentages of jitter.

Despite this, there is always room for improvement. The most natural way to continue this presented work would be to implement the inverse Fourier Slice Theorem within an algorithm in Section 3.2. That is, applying a series of 2D IFFT to a selected projection of the diffracted spectrum every time a 3D IFFT was performed. This modification was indeed the one proposed in [15], but was not performed in this work due to lack of time and the difficulties encountered in the way.

Overall, we can conclude that the results achieved have been satisfactory, given the limitations of the algorithm. The robust power of the Fourier Transform was exploited with its useful application in diffractive imaging. An ideal object was simulated, transformed to the diffractive field, and recovered making use of an algorithm based on the FFT. Furthermore, a new strategy was shown to solve the limitations of the prior algorithm. Though progress can still be made, the potential of Fourier Transform based algorithms for data inversion with Coherent X-ray microscopy has been proven.

References

[1] M. A. Pfeifer, G. J. Williams, I. A. Vartanyants, R. Harder, and I. K. Robinson, “Three-dimensional mapping of a deformation field inside a nanocrystal,” *Nature*, vol. 442, no. 7098, pp. 63–66, 2006.

[2] J. Miao, T. Ishikawa, I. K. Robinson, and M. M. Murnane, “Beyond crystallography: Diffractive imaging using coherent X-ray light sources,” *Science*, vol. 348, no. 6234, pp. 530–535, 2015.

[3] I. Robinson and R. Harder, “Coherent x-ray diffraction imaging of strain at the nanoscale,” *Nature materials*, vol. 8, no. 4, pp. 291–298, 2009.

[4] I. Calvo-Almazán, V. Chamard, T. Grünewald, and M. Allain, “Inhomogeneous probes for bragg coherent diffraction imaging: Toward the imaging of dynamic and distorted crystals,” *Physical Review B*, vol. 110, no. 13, p. 134117, 2024.

[5] T. Latychevskaia, “Iterative phase retrieval in coherent diffractive imaging: practical issues,” *Applied optics*, vol. 57, no. 25, pp. 7187–7197, 2018.

[6] C. E. Shannon, “Communication in the presence of noise,” *Proceedings of the IRE*, vol. 37, no. 1, pp. 10–21, 1949.

[7] D. Sayre, “Some implications of a theorem due to Shannon,” *Acta Crystallographica*, vol. 5, no. 6, pp. 843–843, 1952.

[8] F. J. Ruiz Blasco, “Fourier analysis: Lecture notes,” *Unizar.*

[9] J. Miao, D. Sayre, and H. Chapman, “Phase retrieval from the magnitude of the Fourier transforms of nonperiodic objects,” *JOSA A*, vol. 15, no. 6, pp. 1662–1669, 1998.

[10] E. Hofstetter, “Construction of time-limited functions with specified autocorrelation functions,” *IEEE Transactions on Information Theory*, vol. 10, no. 2, pp. 119–126, 1964.

[11] J. R. Fienup, “Phase retrieval algorithms: a comparison,” *Applied optics*, vol. 21, no. 15, pp. 2758–2769, 1982.

[12] S. Marchesini, H. He, H. N. Chapman, S. P. Hau-Riege, A. Noy, M. R. Howells, U. Weierstall, and J. C. Spence, “X-ray image reconstruction from a diffraction pattern alone,” *Physical Review B*, vol. 68, no. 14, p. 140101, 2003.

[13] R. N. Bracewell, “Strip integration in radio astronomy,” *Australian Journal of Physics*, vol. 9, no. 2, pp. 198–217, 1956.

[14] R. Bracewell, *Fourier analysis and imaging.* Springer Science & Business Media, 2003.

[15] I. Calvo-Almazán, M. Allain, S. Maddali, V. Chamard, and S. Hruszkewycz, “Impact and mitigation of angular uncertainties in bragg coherent x-ray diffraction imaging,” *Scientific Reports*, vol. 9, no. 1, p. 6386, 2019.

[16] A. Ulvestad, Y. Nashed, G. Beutier, M. Verdier, S. Hruszkewycz, and M. Dupraz, “Identifying defects with guided algorithms in bragg coherent diffractive imaging,” *Scientific reports*, vol. 7, no. 1, p. 9920, 2017.

[17] A. Ulvestad, A. Tripathi, S. Hruszkewycz, W. Cha, S. Wild, G. Stephenson, and P. Fuoss, “Chrono CDI: Coherent diffractive imaging of time-evolving samples,” *arXiv:1603.01668v1*, 2016.